Journal Pre-proof

Modeling the mechanical behavior of a helmeted headform impacted with a laminated windshield with consideration of composite failure

Wei Gao, Jiawen Wang, Xiaoqiang He, Y.T. Feng, Shunhua Chen, Chengyong Wang

PII: S0263-8223(21)01232-0
DOI: https://doi.org/10.1016/j.compstruct.2021.114787
Reference: COST 114787

To appear in: *Composite Structures*

Received date : 18 March 2021
Revised date : 24 August 2021
Accepted date : 5 October 2021

Please cite this article as: W. Gao, J. Wang, X. He et al., Modeling the mechanical behavior of a helmeted headform impacted with a laminated windshield with consideration of composite failure. *Composite Structures* (2021), doi: https://doi.org/10.1016/j.compstruct.2021.114787.

Modeling the mechanical behavior of a helmeted headform impacted with a laminated windshield with consideration of composite failure

Wei Gao[a,*], Jiawen Wang[a], Xiaoqiang He[a], Y.T. Feng[b,*], Shunhua Chen[c], Chengyong Wang[a]

[a]*School of Electromechanical Engineering, Guangdong University of Technology, Guangzhou, China*
[b]*Zienkiewicz Centre for Computational Engineering, Swansea University, Swansea, UK*
[c]*School of Marine Engineering and Technology, Sun Yat-sen University, Zhuhai, China*

Abstract

In a bicycle-vehicle or a motorcycle-vehicle accident, the head of an adult rider with a helmet is very likely to impact the windshield laminated glass. Such a complex impact phenomenon normally involves head injury, windshield failure, and helmet damage. The main purpose of this work is to present a computational framework for modeling the impact interaction between a helmeted headform and a windshield glazing. To achieve this, a finite element helmet model is established, where a crushable foam model and a continuum damage mechanics based fracture model are used to describe helmet composite failure. The accuracy of the model is validated by comparing the numerical results with the corresponding experimental data. For the windshield failure, we adopt the commonly used intrinsic cohesive zone model to account for two main failure patterns, i.e., glass fracture and glass-PVB debonding. The mechanical responses of a helmeted headform are compared

*Corresponding author: Wei Gao and Y.T. Feng
Email address: hbweigao@126.com, gaowei@gdut.edu.cn (Wei Gao); y.feng@swansea.ac.uk (Y.T. Feng)

with those of a pure headform to investigate the protective performance of the helmet. Finally, parametric studies are carried out to numerically investigate the effects of impact velocity, helmet posture, and impact location on the windshield on headform response.

Keywords: Head injury, Automotive windshield glazing, Intrinsic cohesive zone model, Helmet composite, Impact interaction

1. Introduction

Motorcycle crash is one of the most common road traffic accidents, accounting for nearly 25% of all road traffic fatalities globally [1]. In Europe, the percentage is 17% in 2014 [2], while in the South-East Asian and Western Pacific Region the percentage is 34% [3]. According to [4], motorcycle crashes in China rose from 37608 in 2015 to 43196 in 2016, and caused 45467 injuries and 10359 deathes in 2015, increasing to 52528 injuries and 11235 deathes in 2016. Injury from motorcycle accident is a considerable cause of deaths and disability in the world and is becoming one of the most serious public health problems, particularly in the developing countries [5].

In a motorcycle accident, the head injury is the main cause of the death of the motorcyclist, because the rider's head takes much high risks for severe or fatal injury in the collision with the road, the vehicle hood and windshield. The frequently used personal equipment – safety helmet, plays an important role to protect the rider's head and brain from injury [1]. It is reported that the safety helmet can reduce the occurrence of head injury by about 60% [6]. Therefore, improving the protective performance of the safety helmet is crucial to protect the rider's head.

In order to improve the protective capability of the safety helmet, impact tests are usually conducted to investigate the mechanical behavior of the safety helmet. These tests can be divided into two categories: (1) the impactor striking the helmeted head or headform, and (2) the helmeted head or headform impacting an obstacle. The first one is usually used to assess the protective capacity of the helmet in some games, e.g. football [7–9], ice hockey [10], heavy industry [11, 12] and combat [13, 14]. However, in the impact test of a bicycle or motorcycle helmet, the helmet often has an initial velocity and impacts onto an obstacle, such as anvil, road and vehicle. The mechanical property of the helmet liner has a significant effect on the energy absorption and the head accelerations under the impact. Many researchers focus on finding a proper liner and shell to promote the protective capability of the helmet. Wen et al. [15] experimentally obtained the energy absorption characteristics of expanded polystyrene (EPS) liners with different densities and found that EPS liners with a density of 0.06 g/cm^3 yielded the best collision energy absorption. Aluminium honeycomb is employed as the reinforcement material of the liner for a better absorption performance of a helmet [16]. The energy absorption of low density polyurea (PU) foams is compared with that of EPS foams [17], and the usage of PU foams as an additional layer on top of the existing EPS liner can reduce the peak acceleration of the headform [17]. Cui et al. [18] designed a functionally graded (FG) foam for helmet liner and found that the FG foam exhibited a much better property of energy absorption than the equivalent uniform foams under low energy impacts. Khosroshahi et al. [19] studied helmet liners with hierarchical lattice architecture and found that this type of liner significantly reduced the peak acceleration of headform in comparison with the traditional EPS liner. Composite materials, such as carbon fibre

reinforcement, were evaluated as an alternative material of the helmet shell with good penetration resistance and ability of absorbing impact energy [20, 21]. Besides, Finan et al. [22] and Petersen et al. [23] reported that the friction coefficient between the helmet and the obstacle had some influence on the head rotational acceleration in the oblique impact, but the influence in the normal impact seemed relatively small. Other conditions, such as impact velocity, impact angle and strap tension, are also considered in the impact between a helmet and an obstacle. For more details on the performance improvement of motorcycle helmets, the reader can refer to a comprehensive review [24].

In a motorcycle or bicycle-vehicle accident, the rider's head has a high possibility to collide with the vehicle windshield [25]. Hence, the response behavior of a pure headform and a helmeted headform impacting onto a windshield is desirable by simulations, because some important parameters, such as absorbed energies of the liner and shell, are difficult to acquire in experiments, but can be obtained easily in numerical simulations. In simulations, modeling laminated glass cracks with a high accuracy is challenging, because the initiation, propagation, closure, and intersection of the cracks need to be considered. The discrete/finte element coupling method (DEM/FEM) [26–31], the element erosion method [32–36] and the cohesive zone method (CZM) [37–43] have been used to model the laminated glass fracture process.

The CZM can be classified into two types according to the insertion instant: extrinsic and intrinsic models. An extrinsic model has been employed to handle the fracture problem of the laminated glass in [40, 41]. In the CZM model, the cohesive elements (CEs) are inserted at a certain instant in a simulation. Therefore, the topological data information needs to be updated adaptively, and the imple-

mentation of the extrinsic CZM is difficult. However, for the intrinsic CZM, CEs are inserted prior to the simulation in the region where the fracture may occur. Recently, the intrinsic CZM has been used to model the cracking of glass layers in the laminated glass plate via ABAQUS, and obtained the results consistent with the experimental outcomes [39]. Later, this intrinsic approach has been further employed for the analysis of the windshield fracture under the impact of human head and headform with consideration of the glass-PVB debonding [37, 38]. The excellent agreement between the simulation and experimental results indicates that the intrinsic CZM is an effective approach for modeling the impact fracture of the windshield glazing.

Thus, in this work, this intrinsic CZM method will be adopted for the glass cracking and PVB-glass debonding of the windshield in the helmet-windshield impact simulations via ABAQUS. A FEM model of a commercial helmet was developed by Ghajari et al. [44, 45] for the usage in LS_DYNA. This helmet model will be employed in our work by transferring the parameter values of the material model for the helmet from LS DYNA to ABAQUS, due to a slight difference of the material models between ABAQUS and LS_DYNA. Then, the helmet model with the transferred parameters will be verified by comparing the numerical results with the experimental observation in the literature [45]. Afterwards, the validated helmet model will be adopted for modeling the response of the helmeted headform impacting on the windshield with consideration of windshield cracking. Besides, to investigate the protective performance of the helmet, the response of the helmeted headform will be compared with that of the pure headform. Finally, the parametric study will be conducted to investigate the effects of the impact velocity, impact location on the helmet, and impact position on a windshield on the

headform response and injury.

2. Intrinsic cohesive zone method

In the cohesive zone method, cohesive elements are inserted on the common surface of two adjacent elements for cracking modeling. There are usually two occasions of inserting CEs: before the damage occurrence during simulation (for extrinsic CZM), prior to simulation (for intrinsic CZM). Because of its easy implementation, the intrinsic CZM is usually used for fracture analysis. The well-

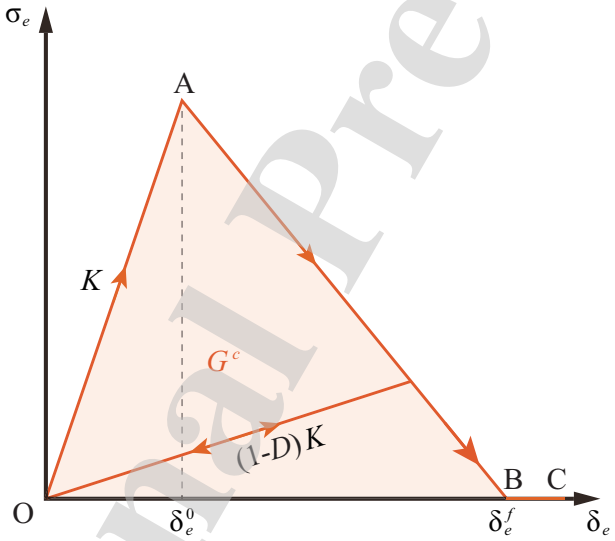

Figure 1: The constitutive law for the bilinear mixed intrinsic model [46, 47].

known bilinear traction-separation model [48] is employed as the constitutive laws of CEs for the glass cracking and PVB-glass debonding. This bilinear mixed-mode model, as shown in Fig. 1, includes three phases: the elastic stage (line *OA*), the damage evolution stage (line *AB*) and the complete failure stage (line *BC*). According to [47], the relation between the equivalent traction σ_e and the

equivalent separation δ_e can be determined from the bilinear curve

$$\sigma_e = (1-D)K\delta_e \tag{1}$$

where K denotes the cohesive stiffness; $D \in [0,1]$ is the degradation coefficient which is equal to zero at the elastic stage and to one at the complete failure stage; δ_e is defined as

$$\delta_e = \left[\langle\delta_1\rangle^2 + \delta_{\text{shear}}^2\right]^{1/2} \tag{2}$$

in which the operator $\langle\square\rangle$ is the Macaulay bracket; δ_1 and δ_{shear} indicate the normal and tangential separations respectively, and δ_{shear} is calculated as:

$$\delta_{\text{shear}} = \left(\delta_2^2 + \delta_3^2\right)^{1/2} \tag{3}$$

In Fig. 1, δ_e^0 and δ_e^f are two important parameters to determine the triangle OAB for the bilinear mixed intrinsic model. δ_e^0 is the equivalent separation at the cracking onset when the following stress criterion is satisfied:

$$\max\left\{\frac{\langle\sigma_1\rangle}{T_1}, \frac{\sigma_2}{T_2}, \frac{\sigma_3}{T_3}\right\} = 1 \tag{4}$$

where T_1, T_2 (or T_3) respectively denote the critical tensile and shear tractions; $T_2 = T_3$ can be considered as T_{shear}; the normal traction σ_1 and tangential tractions σ_2, σ_3 can be written as [49]:

$$\begin{bmatrix}\sigma_1\\ \sigma_2\\ \sigma_3\end{bmatrix} = (1-D)K\begin{bmatrix}\delta_1\\ \delta_2\\ \delta_3\end{bmatrix} - DK\begin{bmatrix}\langle-\delta_1\rangle\\ 0\\ 0\end{bmatrix} \tag{5}$$

The instant of the cracking onset is the ending of the elastic stage, so the degradation coefficient D is still equal to zero. By substituting Eqs. (3)–(5) into Eq. (2),

the effective separation δ_m^0 at the cracking onset can be determined as:

$$\delta_e^0 = \begin{cases} [(\delta_1^0)^2 + \delta_{\text{shear}}^2]^{1/2}, & \text{when } \delta_1 = \delta_1^0 \\ [\delta_1^2 + (\delta_i^0)^2 + \delta_j^2]^{1/2}, & \text{when } \delta_i = \delta_i^0 \ (i,j = 2,3) \end{cases} \tag{6}$$

with

$$\delta_i^0 = \frac{T_i}{K}, \ (i = 1,2,3) \tag{7}$$

The mixed-mode energy release rate G_c can be predicted using a fracture criterion. The following BK criterion proposed by Benzeggagh and Kenane [50] is used in our work

$$G_c = G_1^c + (G_2^c - G_1^c)(\frac{G_2}{G_2 + G_1})^\eta \tag{8}$$

with

$$\begin{cases} G_1 = \frac{1}{2} K \delta_{e1}^f \delta_{e1}^0 \\ G_2 = \frac{1}{2} K \delta_{e2}^f \delta_{e2}^0 \end{cases} \tag{9}$$

in which, η is a material parameter; G_1^c and G_2^c denote the tensile and shear energy release rates respectively; δ_{ei}^f and δ_{ei}^0 $(i = 1,2)$ are the components of δ_e^f and δ_e^0 on the axis δ_i respectively, as displayed in Fig. 2; and G_c represents the area of the triangle OAB as shown in Figs. 1 and 2

$$G_c = \frac{1}{2} K \delta_e^f \delta_e^0 \tag{10}$$

Substituting Eqs. (9)–(10) into Eq. (8) leads to the equivalent separation, δ_e^f, at the complete failure:

$$\delta_e^f = \begin{cases} \frac{2}{K\delta_e^0}[G_1^c + (G_2^c - G_1^c)(\frac{\beta^2}{1+\beta^2})^\eta], & \text{when } \delta_1 > 0 \\ \delta_2^f, & \text{when } \delta_1 \le 0 \end{cases} \tag{11}$$

with the mode mixity ratio β defined to be

$$\beta = \tan(\theta) = \frac{\delta_{\text{shear}}}{\delta_1} = \frac{\delta_{e2}^0}{\delta_{e1}^0} = \frac{\delta_{e2}^f}{\delta_{e1}^f} \tag{12}$$

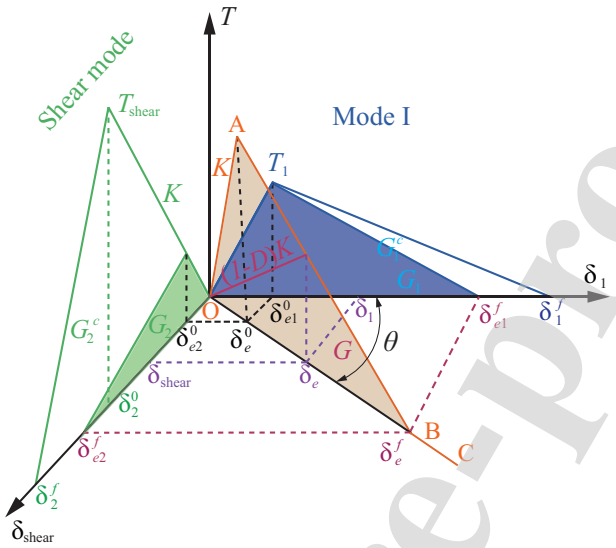

Figure 2: The constitutive law for the bilinear mixed intrinsic model[37, 47].

The change of β results in the variation of δ_e^f. Therefore, δ_e^f and the triangle OAB in Figs. 1 and 2 are updated at every time step. Due to the irreversibility of the material damage, the degradation coefficient D increase monotonically

$$D = \max\{D_{\text{new}}, D\} \tag{13}$$

with

$$D_{\text{new}} = \begin{cases} \frac{\delta_e^f(\delta_e - \delta_e^0)}{\delta_e(\delta_e^f - \delta_e^0)}, & \text{when } \delta_e^0 < \delta_e < \delta_e^f \\ 0, & \text{when } \delta_e < \delta_e^0 \text{ or } \delta_e > \delta_e^f \end{cases} \tag{14}$$

3. Model and validation

3.1. Hybrid II headform

A hybrid II headform developed by Ghajari et al. [45] is adopted for the helmet-windshield impact simulation using ABAQUS. The headform with a mass of 4.79 kg consists of a mass block and a layer of rubber skin. The mass block is tied with the inner surface of the skin. The rubber skin is divided into C3D8 and C3D6 elements, and the Ogden model is used for the modeling of the rubber skin [45, 51]. Due to the format difference of the Ogden model used in these two pieces of FEM software, the material parameters in LS_DYNA cannot be used in ABAQUS directly.

In our work, the nominal stress versus loading-direction stretch curves (shown in Fig. 3) in uniaxial, equibiaxial and planar modes are derived from the format of the Ogden model [52, 53] used in LS_DYNA. Then, these curves and Poisson's ratio are employed as the input parameters for the Ogden model in ABAQUS.

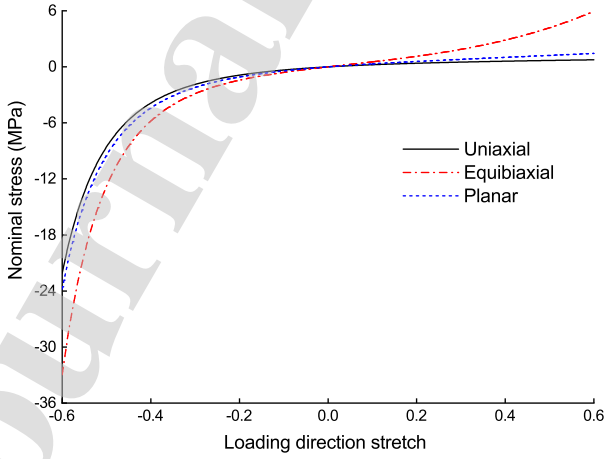

Figure 3: The nominal stress versus loading-direction stretch curves as the input data of the Ogden model for ABAQUS

Table 1: The viscoelastic parameters of the rubber skin

Parameter	i=1	i=2	i= 3	i=4	i=5	$i=\infty$
G_i (MPa)	0.028	0.065	0.087	0.172	0.235	0.902
τ_i (s)	100.0	10.0	1.0	0.1	0.01	0.0

In order to consider the viscoelasticity of the skin, the shear relaxation modulus $G(t)$ can be written via the generalized Maxwell model as

$$G(t) = G_\infty + \sum_{i=1}^{n} G_i e^{-t/\tau_i} \tag{15}$$

where t is the current time; G_∞ denotes the long-term shear relaxation modulus; and G_i and τ_i are the optional shear modulus and relaxation time for the i^{th} term respectively, whose values are listed in Table. 1.

3.2. The validation of helmet model

The helmet used in the impact experiments by Ghajari et al. [44, 45] consists of an outer composite shell, several inner foam liners and a chin strap, and was modeled by using LS_DYNA. This helmet model is adopted in our work and the material parameters of the foam liners and composite shell need to be transferred to ABAQUS.

The inner foam liners with nonlinear mechanical behavior [54] are capable of absorbing the impact energy, increasing the distance and time period over which the human head stops, and thereby reducing the impact force and accelerations of the human head [24]. The crushable foam model with volumetric hardening available in ABAQUS is preferable for the liner foam analysis. It has five parameters, density ρ_{fm}, Young's modulus E_{fm}, Poisson's ratio v_{fm}, compression yield stress ratio k_{fm} and hydrostatic yield stress ratio k^t_{fm}.

The values of these parameters for the top, main and cheek-chin foams used in our work can be obtained by transferring the foam model parameters used in LS_DYNA provided by Ghajari et al. [44, 45]. The compression yield stress ratio k_{fm} and hydrostatic yield stress ratio k^t_{fm} can be obtained by

$$\begin{cases} k_{\text{fm}} = \dfrac{\sigma_c^0}{p_c^0} \\ k^t_{\text{fm}} = \dfrac{p_t}{p_c^0} \end{cases} \tag{16}$$

where σ_c^0 and p_c^0 denote the parameters of the foam model used in LS_DYNA, i.e. the initial yield stresses in uniaxial and hydrostatic compression, respectively; and p_t is the yield strength in hydrostatic tension. The parameter values of the foam model in ABAQUS are listed in Table 2. The chin strap is modelled as an elastic material with a density 870 kg/m^3, Young's modulus 1.0 GPa, and Possion's ration 0.3.

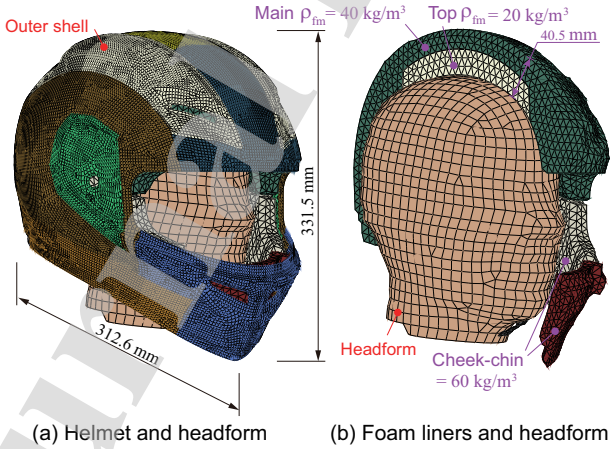

Figure 4: The helmet and its foam liners with hybrid II headfoam.

The outer shell of the helmet (see Fig. 4) is a fiber-reinforced composite composed of several different laminas which provide the support for the inner liners

Table 2: The parameters and their values of the foam model in ABAQUS

Position	ρ_{fm} (kg/m^3)	E_{fm} (MPa)	v_{fm}	k_{fm}	k^t_{fm}
Top	20	2.9	0.001	1.07515	1.18617
Main	40	10.6	0.001	1.07706	2.65256
Cheek-chin	60	23.2	0.001	1.08793	0.85697

and spread the impact load over the liners [24]. In each lamina, the fibers are arranged along a certain direction in the matrix. The initial damage criterion of the lamina used in ABAQUS is as follows:

for fiber

$$\begin{cases} \left(\frac{\sigma_{11}}{X_T}\right)^2 + \alpha\left(\frac{\sigma_{12}}{S_L}\right)^2 \geq 1, & \text{if } \sigma_{11} \geq 0 \text{ (tension)} \\ \left(\frac{\sigma_{11}}{X_C}\right)^2 \geq 1, & \text{if } \sigma_{11} < 0 \text{ (compression)} \end{cases} \tag{17}$$

for matrix

$$\begin{cases} \left(\frac{\sigma_{22}}{Y_T}\right)^2 + \left(\frac{\sigma_{12}}{S_L}\right)^2 \geq 1, & \text{if } \sigma_{22} \geq 0 \text{ (tension)} \\ \left(\frac{\sigma_{22}}{2S_T}\right)^2 + \left[\left(\frac{Y_C}{2S_T}\right)^2 - 1\right]\frac{\sigma_{22}}{Y_C} + \left(\frac{\sigma_{12}}{S_L}\right)^2 \geq 1, & \text{if } \sigma_{22} < 0 \text{ (compression)} \end{cases} \tag{18}$$

In the above equations, the subscripts 1 and 2 denote the fiber and matrix directions, respectively; X_T and S_L are the tension and compression strengthes along the fiber direction respectively; Y_T and Y_C denote the tension and compression strengthes of the matrix, respectively. When α and S_T are set to be zero and $0.5Y_C$ respectively, Eqs. (17-18) will be similar to those employed in LS_DYNA. The parameters of the glass/epoxy layer in our work is listed in Table 3. Glass epoxy composites have a nonlinear mechanical behavior in shear loading, and the reader can refer to [55, 56] for more details.

Table 3: The parameters and their values of the glass/epoxy layer [44].

Parameters	Values
Density ρ	1984 kg/m^3
Young's modulus along fiber direction E_1	46 GPa
Young's modulus E_2 along matrix direction	16 GPa
Poisson's ratio ν_{12}	0.1
Shear modulus G_{12}	5.8 GPa
Shear modulus G_{13}	5.8 GPa
Shear modulus G_{23}	5.8 GPa
Tension strength along fiber direction X_T	1280 MPa
Compression strength along fiber direction X_C	800 MPa
Tension strength along matrix direction Y_T	40 MPa
Compression strength along matrix direction Y_C	145 MPa
S_L	73 MPa
S_T	72.5 MPa ($0.5Y_C$)
α	0.0
Fracture energy density for fiber tension mode	30.9 mJ/mm^3
Fracture energy density for fiber compression mode	12.1 mJ/mm^3
Fracture energy density for matrix tension mode	5.8 mJ/mm^3
Fracture energy density for matrix compression mode	2.1 mJ/mm^3

Table 4: The element number and types used in each component of the helmet model

Components	Element type	Element number
Composite shell	S4RS and S3RS	24162
Foam liner	C3D4	39804
Chin strap	S4RS and S3RS	296

Although the critical energy release rate of each layer for the composite shell can be set to be equal, the damage evolution laws used in those two pieces of FEM software are different. The bilinear law [57] different from the exponential one in LS_DYNA is adopted for the damage evolution via ABAQUS in our work. To verify the helmet model in ABAQUS, the impact process of the helmet with the Hybrid II headform is considered. Initially, these helmet and headform impact onto a fixed and rigid flat anvil with a velocity of 8.5 m/s and there is a 165° angle between the initial velocity and the normal of the flat anvil, as shown in Fig. 7(a). The element number and types in each component of the helmet model are listed in Table 4. The material parameters in Table 1, 2 and 3 are adopted for the analysis of the corresponding components in the helmet and headform. The contact interactions may occur between the components whose friction coefficients are depicted in Table 5.

The linear and rotational acceleration histories are compared with the simulation results and the experimental observations in [45], as shown in Figs. 5-6. We can see that the acceleration histories are consistent with the results in the literature [45]. In addition, the positions and postures of the helmet at four time instants are displayed in Fig. 7 and compared with the simulation results and the experimental observations in [45]. The computational results are consistent

Table 5: The friction coefficients between the contact components in the helmet-anvil impact system

Component	Component	Coefficients
Composite shell	Flat anvil	0.55 [45]
Head skin	Foam liner	0.5 [58]
Composite shell	Foam liner	0.5 [44]
Chin strap	Head skin	0.5
Chin strap	Foam liner	0.5
Foam liner	Foam liner	1.0

with the experimental ones. These good agreements indicate that the helmet and the hybrid II headform can be used in helmet-windshield impact simulations via ABAQUS.

3.3. Windshield model

The windshield glazing is composed of double outer glass layers bonded by a single inner PVB layer. The intrinsic CZM is considered to be an effective method to model the glass fracture and gradual debonding between glass and PVB [37–39].

To model glass cracking, the glass layers are divided into many solid elements, and intrinsic CZM elements are inserted on the common surfaces of adjacent solid elements prior to simulations [37–39]. In addition, intrinsic CZM elements were also employed to bond the glass and PVB layers [37, 38], so the PVB-glass gradual debonding were considered naturally. In these references, the accuracy and effectiveness of the windshield model were validated by comparing the simulation results of the headform impact with the corresponding experimental outcomes.

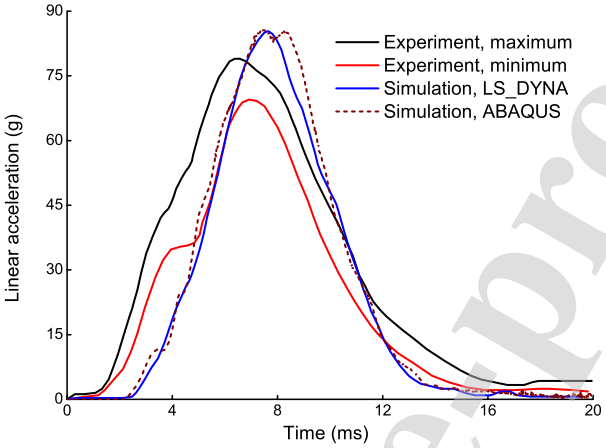

Figure 5: The comparison of the linear acceleration histories of the helmeted headform with the simulation results and experimental outcomes in [45].

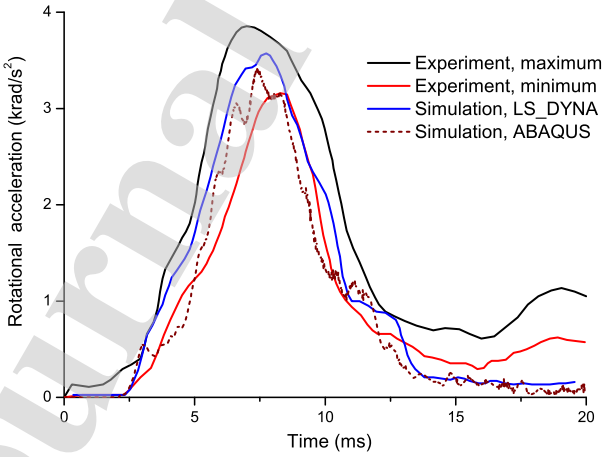

Figure 6: The comparison of the rotation acceleration histories of the helmeted headform with the simulation results and experimental outcomes in [45].

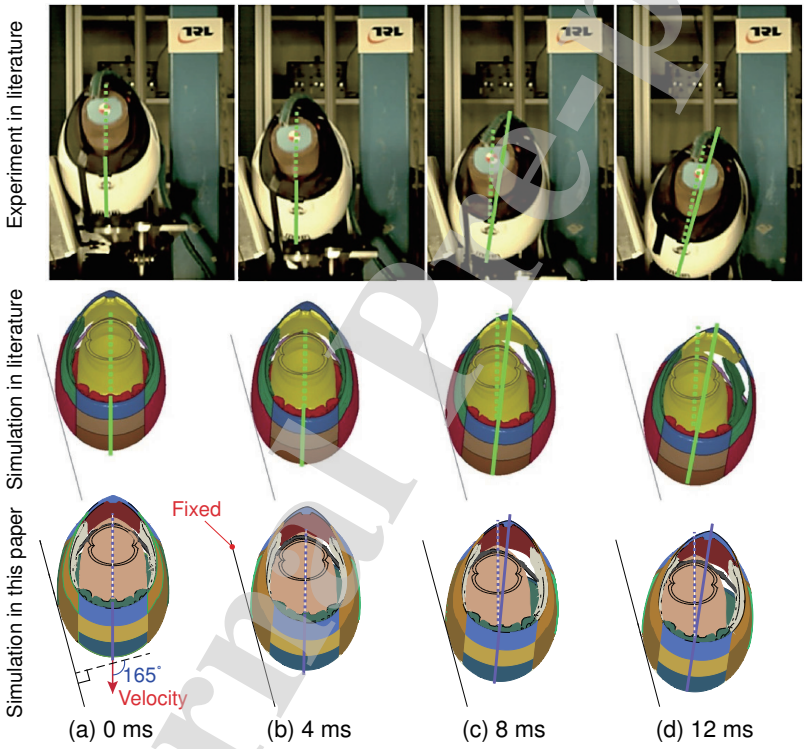

Figure 7: The comparison of the headform and helmet positions between our numerical results, the simulation and experimental results in the literature [45].

Table 6: Material models and parameters used for the supporter and all components of the windshield glazing.

Structure	Material model [59]	Parameters
Glass	Linear elastic	ρ = 2500 kg/m^3, E = 70 GPa, ν = 0.23 [39, 40]
PVB	Viscoelastic	ρ = 1100 kg/m^3, K_0 = 2.0 GPa, G_0 = 146.12 MPa, G_∞ = 0.15 MPa [60]
Glass cracking	CZM	$T_1 = T_2 = T_3$ = 60 MPa, K = 500 GPa/mm, η = 0.3, G_1^c = 10 N/m, $G_2^c = G_3^c$ = 50 N/m [39, 40, 61, 62]
PVB-glass debonding	CZM	$T_1 = T_2 = T_3$ = 10 MPa, K = 1.252 GPa/mm, η = 0.3, $G_1^c = G_2^c = G_3^c$ = 300.75 N/m [60, 63, 64]
Supporter	Mooney-Rivlin	ρ = 1200 kg/m^3, ν = 0.49, C_{10} = 0.5 MPa, C_{01} = 4.2 MPa [38, 65]

Hence, this windshield model is adopted in this paper. The material model and parameters for each component of the windshield glazing are depicted in Table 6, which are the same as those used in [37, 38].

4. Parametric studies

In order to investigate the protection performance of a helmet, the impact processes of both pure hybrid II headform and helemeted headform (validated in Section 3.2) onto a windshield are considered numerically in this section. The headform, helmet and windshield models described in Section 3 are used in the simulations. An annular rubber strip, named supporter, has a fixed bottom surface, and the strip's top surface is tied with the bottom of the windshield model [37, 38]. This supporter is analyzed by Mooney-Rivlin model with the material parameters

as listed in Table 6.

4.1. Effect of impact velocity

Based on [37, 38, 66], four impact velocities, 5.5 m/s (20 km/h), 8.3 m/s (30 km/h), 11.1 m/s (40 km/h) and 13.9 m/s (50 km/h) are adopted for the impactors (i.e. pure and helmeted headforms). The windshield model described in Section 3.3 is used in the simulations. Initially, the pure headform or the helmeted one is just above the windshield center and then will be in contact with the top surface of the windshield. The friction coefficient between the impactors and the windshield is set to be 0.2 [67].

The acceleration-history curves of the pure headform are plotted in Fig. 8. Each curve has two main peaks, with the first peak much higher than the second one. Besides, a larger impact velocity leads to a higher first and second peaks and a larger HIC value, as given in Table 7.

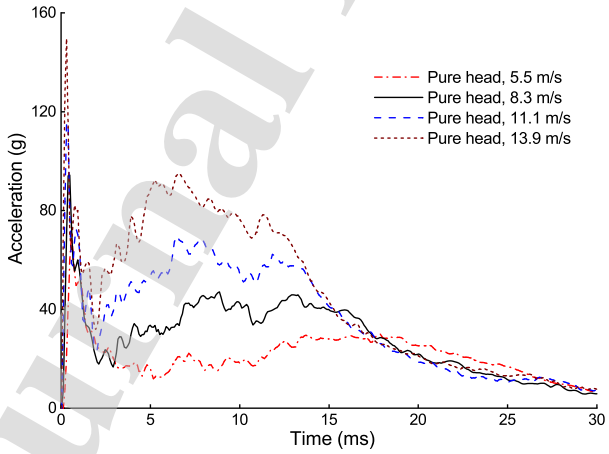

Figure 8: The acceleration history curves of the pure headform with different initial velocities.

The acceleration history curves of the helmeted headform are displayed in Fig. 9. In the first 10 milliseconds, the curve for a larger impact velocity tends to reach

higher peaks and has a larger acceleration. After 24 ms, the difference becomes small. The highest peak values of the acceleration curves of 5.5 m/s, 8.3 m/s, 11.1 m/s and 13.9 m/s in Fig. 9 are respectively 19.6%, 33.0%, 39.0% and 41.8% smaller than the counterparts in Fig. 8, because the foam liners in the helmet provide a cushion for the headform during the impact process. This indicates that the helmet can reduce the head maximum acceleration (which has significant effects on head injury), and that the higher the impact velocity is, the larger the reduction of the head maximum acceleration. The HIC values are calculated from these acceleration curves and listed in Table 7. As shown in this table, wearing helmet can reduce the HIC value under a high velocity impact, i.e. reducing by 40.3 and 74.4 at the impact velocities 11.1 m/s and 13.9 m/s.

However, at a relatively small impact velocity, the helmet almost contributes no reduction to the HIC value. The similar results are also observed in the experiments in [68].

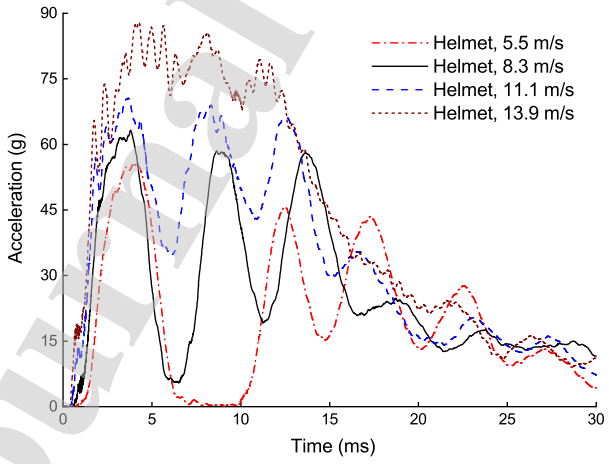

Figure 9: The acceleration histories of the helmeted headform under different-velocity impacts.

The crack patterns of the windshield glazing under the helmeted and pure

Table 7: The calculated HIC values for the pure headform and helemeted headform with different initial velocities

Impactor	Velocity	Initiation	Termination	HIC	HIC variation
Pure head	5.5 m/s	6.12 ms	21.12 ms	43.1	
Wear helmet	5.5 m/s	10.82 ms	25.82 ms	46.5	3.4
Pure head	8.3 m/s	0.20 ms	15.20 ms	136.2	
Wear helmet	8.3 m/s	1.5 ms	16.50 ms	132.5	-3.7
Pure head	11.1 m/s	0.13 ms	15.13 ms	333.1	
Wear helmet	11.1 m/s	1.50 ms	16.50 ms	292.8	-40.3
Pure head	13.9 m/s	0.10 ms	15.10 ms	661.2	
Wear helmet	13.9 m/s	1.40 ms	16.40 ms	586.8	-74.4

headforms with different initial velocities are shown in Fig. 10. We can see that the headform with a large initial velocity tends to result in a large cracking area of the windshield glazing. Besides, the helmeted headform impact tends to result in slightly more cracks in the windshield than those of the pure headform impact, but the difference is not obvious.

Fig. 11 shows the internal energy evolution histories of the foam liners in the helmet with different velocities. These curves have similar tendency, namely rising quickly in the beginning, then having some fluctuations, and finally converging to a constant. The foam liners absorb more energy under the impact with a higher velocity. Besides, for the helmeted headform with the initial velocity of 8.9 m/s, three main peaks appear on the internal energy history of the foam liners in Fig. 11 and also on the acceleration history of the headform in Fig. 9 almost at the same time. The similar phenomenon can also be observed for the cases with

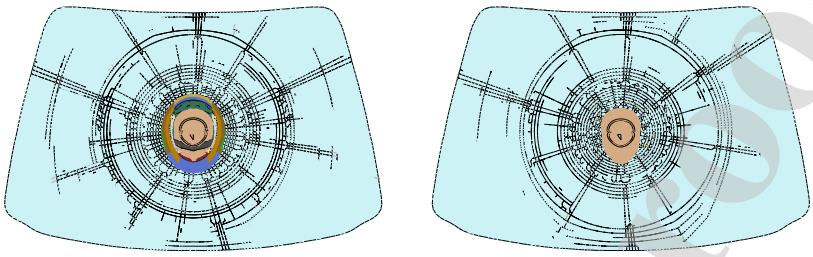

(a) 5.5 m/s

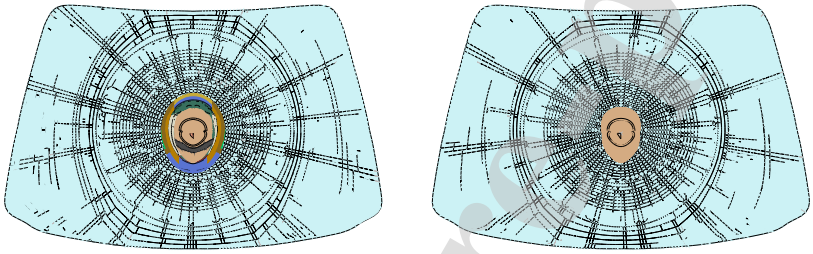

(b) 8.3 m/s

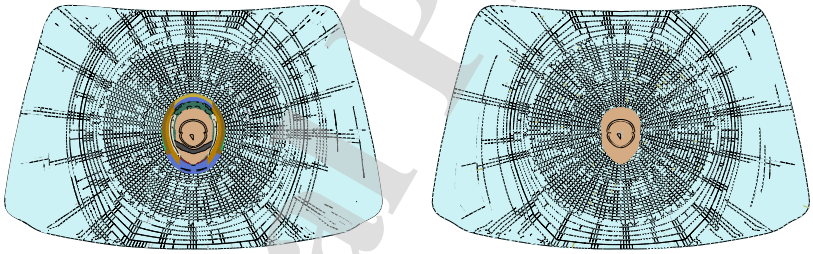

(c) 11.1 m/s

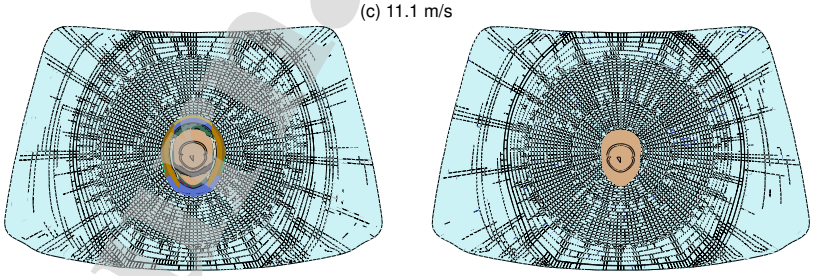

(d) 13.9 m/s

Figure 10: The crack patterns of the windshield (viewed from impact side) under the impact of the pure and helmeted headforms at velocities of (a) 5.5 m/s, (b) 8.3 m/s (c) 11.1 m/s (d) 13.9 m/s.

other initial velocities. This indicates that the foam liners have important effects on the acceleration of the helmeted headform.

The internal energies of the helmet shell under different-velocity impacts are shown in Fig. 12. The internal energies rise to considerably large values and then decrease quickly in the beginning, then fluctuate and finally keep almost constant. The helmet shell under a high-velocity impact has a large internal energy. In comparison with the internal energies of the foam liners in Fig. 11, the internal energy of the helmet shell is not negligible in the beginning, but it only lasts for a short period of time and becomes relatively small after 4 ms. In other words, the helmet shell absorbs the initial shock in an accident, but finally absorbs only a small amount of energy [24, 69, 70].

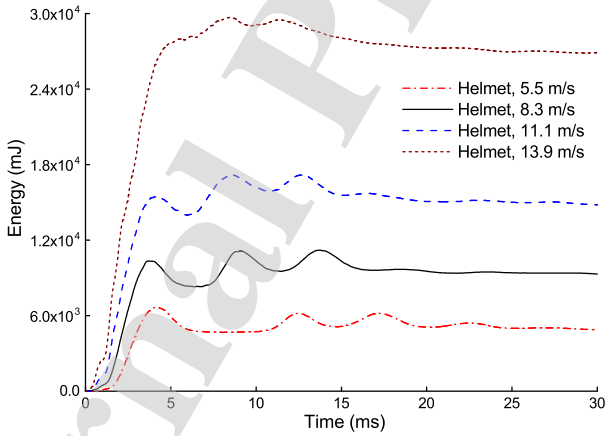

Figure 11: The internal energy histories of the foam in the helmet with different velocities.

4.2. *Effect of helmet impact position*

The crown, front, lateral and rear impacts are generally used to investigate the response of a helmeted headform. Here, we consider four cases, i.e. front, crown, laterial, and rear impacts. The corresponding postures and impact positions on the

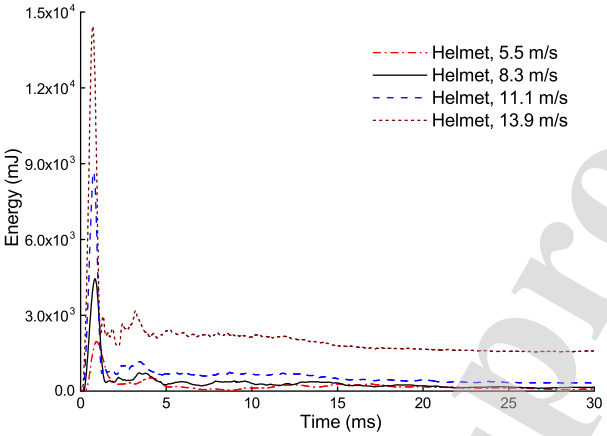

Figure 12: The internal energy of the helmet shell with different velocities.

helmets are displayed in Fig. 13. The helmet and headform in each case have the same initial velocity of 11.1 m/s along the normal direction of the windshield at the impact point. Except for the posture of the helmeted headform and the impact positions on the helmet, other conditions and parameters are the same as the case with the same velocity in Section 4.1.

The (linear) acceleration histories of the headform are displayed in Fig. 14. In this figure, the curves of the headform with different postures have a similar tendency, namely increasing quickly in the beginning, following by three main wave crests, and then decreasing after 24 ms. The lateral impact tends to yield large peak values, while the front, crown and rear impacts have small ones. The similar phenomenon is also observed in the impact of the helmeted headform onto the anvil [71]. The reason may be that the stiffer foam at the lateral position results in the relatively small energy absorbed by the foam liners under the lateral impact than those under other impacts, as shown in Figs. 15. The internal energy of the composite shell is shown in Fig. 16. Compared with the foam's internal energy in

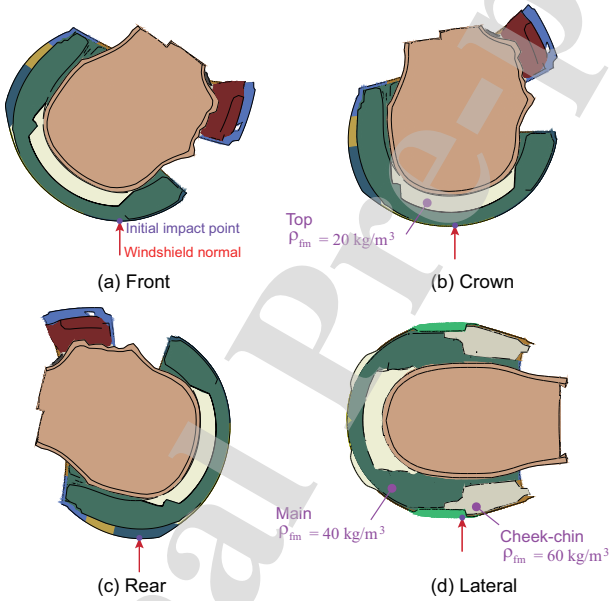

Figure 13: The initial posture of the helmeted headform (whose front half is hidden) for (a) crown, (b) front, (c) lateral and (d) rear impacts.

Fig. 15, the internal energy of the composite shell is nontrivial in the beginning. But the internal energy of the shell is much smaller than that of the foam liners after 7 ms. This indicates that during this time period the foam liners absorb more energy than the composite shell.

The HIC value of the lateral impact is relatively larger than those of the other cases which have negligible differences, as shown in Table 8. Due to the different postures of the helmeted headform, the rotational acceleration histories of the headform are plotted in Fig. 17. This figure shows that the lateral impact leads to the largest peak values of the rotational acceleration histories, while the crown impact yields the smallest ones. Therefore, the crown impact instead of the other impacts is considered in Sections 4.1 and 4.3.

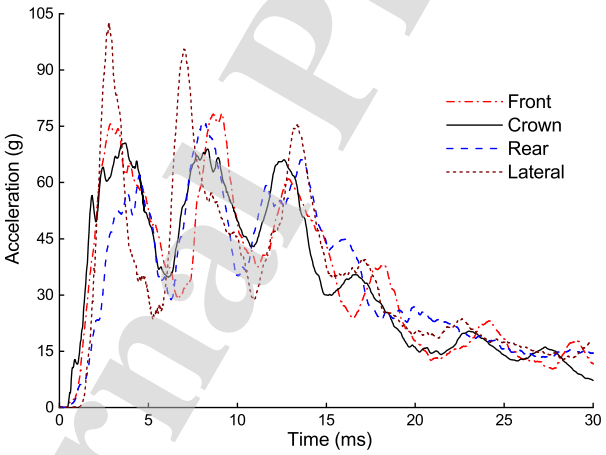

Figure 14: The acceleration histories of the headform under the crown, front, lateral and rear impacts.

4.3. Effect of windshield impacted location

In order to investigate the effects of the impact location on the windshield, the helmeted headform impacting six positions, as displayed in Fig. 18, are consid-

Table 8: The calculated HIC values of the crown, front, lateral and rear impacts

Location	Initiation	Termination	HIC
Front	1.48 ms	16.48 ms	275.2
Crown	1.50 ms	16.50 ms	292.8
Rear	2.37 ms	17.37 ms	271.4
Lateral	2.00 ms	17.00 ms	292.6

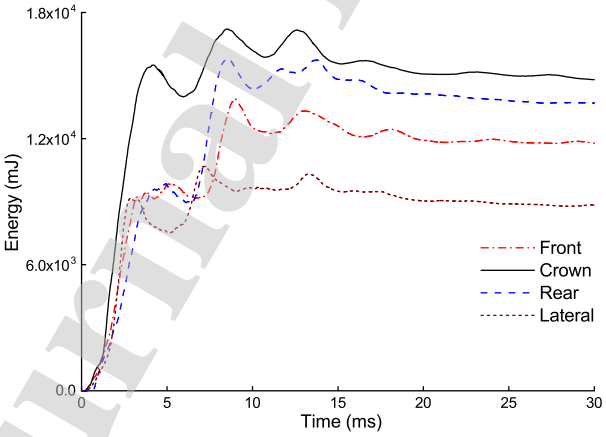

Figure 15: The internal energy histories of the foam liner for the crown, front, lateral and rear impacts.

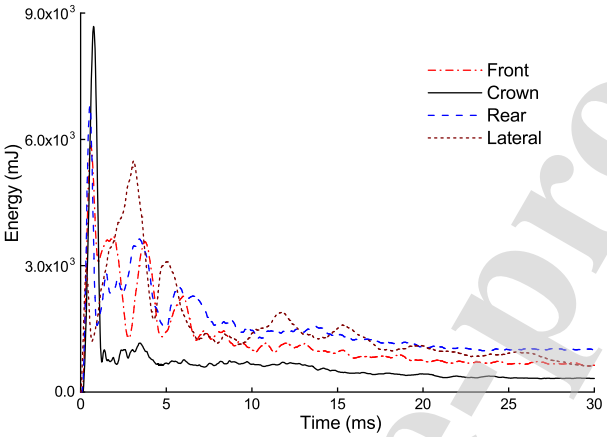

Figure 16: The internal energy histories of the composite shell under the crown, front, lateral and rear impacts.

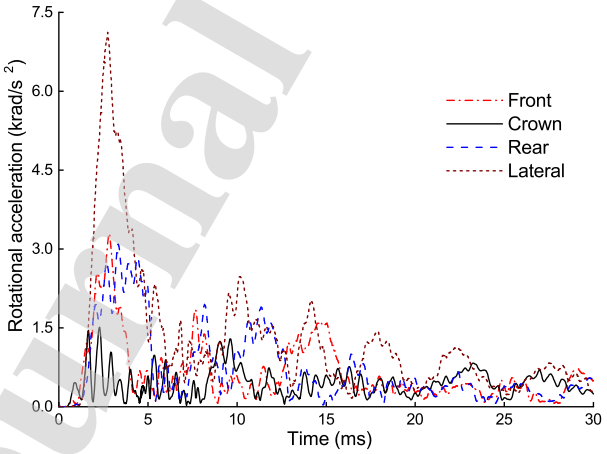

Figure 17: The rotational acceleration histories of the headform for the crown, front, lateral and rear impacts.

ered. In each case, the helmet and headform with an initial velocity of 11.1 m/s come into collision with the windshield along its normal direction. To improve both analysis accuracy and computational efficiency, the region of the windshield surrounding the impact location is discretized into a finer mesh, while a coarser mesh is used elsewhere. The friction coefficient between the helmet and the windshield is set to be 0.2 [67].

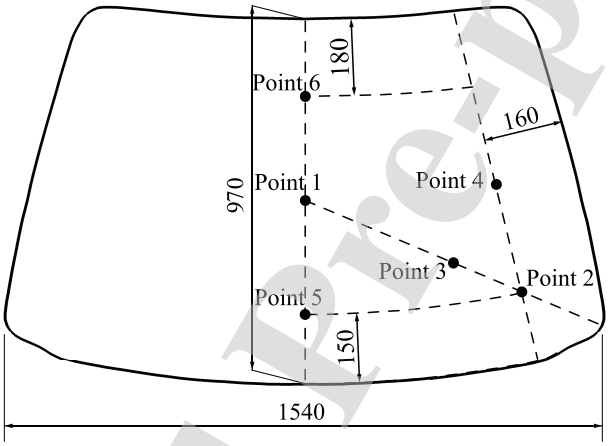

Figure 18: The impacted positions on the windshield in the six numerical cases (unit:mm).

The head acceleration histories of the six cases are displayed in Fig. 19. The head acceleration curves for the impact points 1 and 3 have several main peaks, while only two main peaks appears on the other curves. The impact points 1 and 3 yield a small difference between the first and second peak values, but the impact points 2, 4 and 5 have much larger second peaks than the first ones. In Fig. 19 the impact points are arranged according to the second peak values (from the large to small) as: points 2, 5 or 4, 6, 1 or 3. The same sequence is also used in Table. 9. From these results, we can conclude that the impact location closer to the supporter tends to result in a larger value of the second peak and HIC.

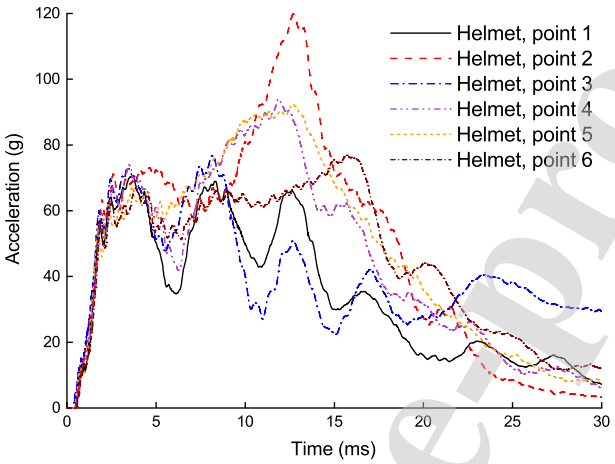

Figure 19: The linear acceleration histories of the helmeted headform impacting onto the different positions of the windshield.

Table 9: The calculated HIC values for the case at different impact positions on the windshield

Point	Initiation	Termination	HIC
2	2.36 ms	17.36 ms	787.4
5	2.10 ms	17.10 ms	669.5
4	1.78 ms	16.78 ms	587.9
6	2.34 ms	17.34 ms	492.0
1	1.50 ms	16.50 ms	292.8
3	1.47 ms	16.47 ms	267.8

The internal energy histories of the form liners in the cases with different locations on the windshield are displayed in Fig. 20. This figure shows that the internal energy histories for the impact points 1 and 3 have a similar tendency, but are different from the other four impact points. The impact location closer to the supporter is inclined to result in a larger internal energy of the foam liner after 15 ms. The possible reason is that the supporter constrains the displacement of the windshield, which results in a high contact force between the headform and the foam liner. The internal energy histories of the composite shell are displayed in Fig. 21, in which the curve of the case closer to the impact location to the supporter tends to fluctuate more severely during the time period between 10 ms and 20 ms.

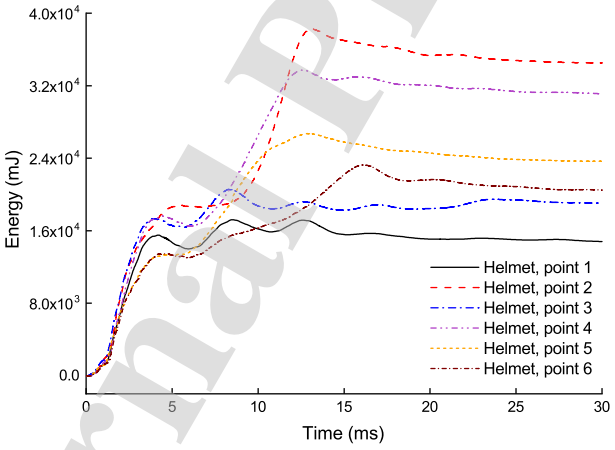

Figure 20: The internal energy histories of the form liner for the cases with the different positions on the windshield.

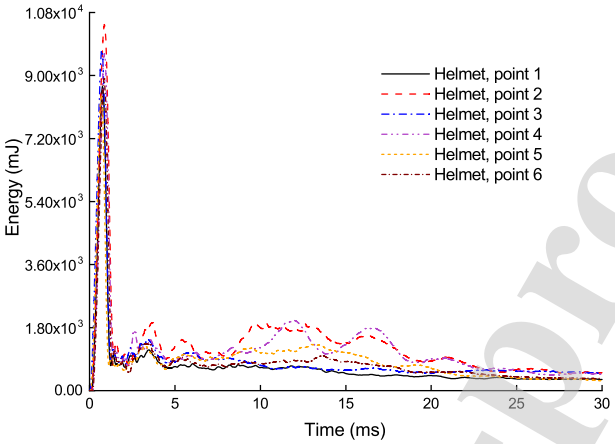

Figure 21: The internal energy histories of the composite shell for the cases with the different positions on the windshield.

5. Conclusions

The impact behavior of the helmeted headform onto the windshield is investigated numerically. The accuracy and validity of the helmet model are demonstrated by the good agreement between the simulated results and the existing experimental observations. Then, the validated helmet model is used to perform parametric studies. The effects of the parameters, including the posture of the helmet headform, the impact velocity and the impact locations on the windshield, are investigated numerically. In addition, the headform response between the pure headform and the helmeted headform impacts are compared. The parametric simulation results are summarized as:

(1) The impact velocity has crucial effects on the headform acceleration and HIC values. A higher impact velocity tends to result in a larger acceleration of the headform and HIC values for both pure and helmeted headforms. Compared with the pure headform impact, the helmet reduced the maximum

acceleration by 19.6%, 33.0%, 39.0% and 41.8% at the impact velocities of 5.5 m/s, 8.3 m/s, 11.1 m/s and 13.9 m/s, respectively; and under a relatively high velocity impact, the helmet tends to decrease the HIC values of the headform, e.g. reducing by 40.3 and 74.4 at the impact velocities 11.1 m/s and 13.9 m/s.

(2) The impact location on the windshield has significant influences on the response of the helmeted headform. The impact location closer to the supporter tends to result in higher peak values of headform acceleration histories and a larger HIC value.

(3) The stiffer foam liner at the lateral positions leads to relatively larger accelerations in the lateral impact than the front, crown and rear impacts. In the beginning of impact, the absorbed energy by the composite shell is non-negligible in comparison with the foam liners. However, after the instant of 4 ms, the foam liners absorb much more energy.

Acknowledgements

Dr. Wei Gao would like to acknowledge the financial support of NNSF of China (Nos. 51878184 and 51404209). The authors thank Dr Mazdak Ghajari from Imperial College London UK, for providing the FEM models of the helmet and headform.

References

[1] C. Ding, M. Rizzi, J. Strandroth, U. Sander, N. Lubbe, Motorcyclist injury risk as a function of real-life crash speed and other contributing factors, Accident Analysis & Prevention 123 (2019) 374–386.

[2] EC, Traffic safety basic facts 2016: Motorcycles and mopeds, 2016.

[3] W. H. Organization, Global status report on road safety 2015, World Health Organization, 2015.

[4] Y. Xiao, H. Huang, Y. Peng, X. Wang, A study on motorcyclists head injuries in car–motorcycle accidents based on real-world data and accident reconstruction, Journal of Mechanics in Medicine and Biology 18 (2018) 1850036.

[5] P. K. Sisimwo, G. M. Onchiri, Epidemiology of head injuries and helmet use among motorcycle crash injury: a quantitative analysis from a local hospital in Western Kenya, The Pan African Medical Journal 31 (2018).

[6] T. M. Rice, L. Troszak, J. V. Ouellet, T. Erhardt, G. S. Smith, B.-W. Tsai, Motorcycle helmet use and the risk of head, neck, and fatal injury: Revisiting the hurt study, Accident Analysis & Prevention 91 (2016) 200–207.

[7] S. Rowson, S. M. Duma, R. M. Greenwald, J. G. Beckwith, J. J. Chu, K. M. Guskiewicz, J. P. Mihalik, J. J. Crisco, B. J. Wilcox, T. W. McAllister, et al., Can helmet design reduce the risk of concussion in football?, Journal of neurosurgery 120 (2014) 919–922.

[8] T. Darling, J. Muthuswamy, S. Rajan, Finite element modeling of human brain response to football helmet impacts, Computer methods in biomechanics and biomedical engineering 19 (2016) 1432–1442.

[9] E. T. Campolettano, R. A. Gellner, D. W. Sproule, M. T. Begonia, S. Rowson, Quantifying youth football helmet performance: assessing linear and rotational head acceleration, Annals of biomedical engineering 48 (2020) 1640–1650.

[10] J. M. Clark, T. B. Hoshizaki, M. D. Gilchrist, Protective capacity of an ice hockey goaltender helmet for three events associated with concussion, Computer methods in biomechanics and biomedical engineering 20 (2017) 1299–1311.

[11] M. Lakshmanan, D. Prathamesh, Analysis of industrial safety helmet under low-velocity impact, Journal of failure analysis and prevention 20 (2020) 85–94.

[12] J. Z. Wu, C. S. Pan, B. M. Wimer, C. L. Rosen, Finite element simulations of the head–brain responses to the top impacts of a construction helmet: Effects of the neck and body mass, Proceedings of the Institution of Mechanical Engineers, Part H: Journal of engineering in medicine 231 (2017) 58–68.

[13] J. Yang, J. Dai, Simulation-based assessment of rear effect to ballistic helmet impact, Computer-Aided Design and Applications 7 (2010) 59–73.

[14] K. M. Tse, L. B. Tan, B. Yang, V. B. C. Tan, H. P. Lee, Effect of helmet liner systems and impact directions on severity of head injuries sustained in bal-

listic impacts: a finite element (FE) study, Medical & biological engineering & computing 55 (2017) 641–662.

[15] W.-c. Wen, Y.-x. Li, D.-m. Fu, Study on impact energy absorbing performance of EPS buffer layer of motorcycle helmet, in: 2013 International Conference on Mechanical and Automation Engineering, IEEE, 2013, pp. 105–109.

[16] G. D. Caserta, L. Iannucci, U. Galvanetto, Shock absorption performance of a motorbike helmet with honeycomb reinforced liner, Composite Structures 93 (2011) 2748–2759.

[17] B. Ramirez, O. Kingstedt, R. Crum, C. Gamez, V. Gupta, Tailoring the rate-sensitivity of low density polyurea foams through cell wall aperture size, Journal of Applied Physics 121 (2017) 225107.

[18] L. Cui, S. Kiernan, M. D. Gilchrist, Designing the energy absorption capacity of functionally graded foam materials, Materials Science and Engineering: A 507 (2009) 215–225.

[19] S. F. Khosroshahi, S. Tsampas, U. Galvanetto, Feasibility study on the use of a hierarchical lattice architecture for helmet liners, Materials Today Communications 14 (2018) 312–323.

[20] B. Fuernschuss, E. Kandare, A. Sabo, T. Y. Pang, Rethinking the safety of jockey helmets: a statistical comparison of different composite laminate helmet shells, Procedia engineering 147 (2016) 507–512.

[21] W. Berata, Sutikno, A. Safa'at, J. A. Nugroho, Multiple reinforcements composite as a lightweight helmet material in order to absorb impact energy due

to collision, in: AIP Conference Proceedings, volume 1983, AIP Publishing LLC, 2018, p. 050011.

[22] J. D. Finan, R. W. Nightingale, B. S. Myers, The influence of reduced friction on head injury metrics in helmeted head impacts, Traffic injury prevention 9 (2008) 483–488.

[23] P. G. Petersen, L. V. Smith, D. Nevins, The effect of surface roughness on oblique bicycle helmet impact tests, Proceedings of the Institution of Mechanical Engineers, Part P: Journal of Sports Engineering and Technology 234 (2020) 320–327.

[24] F. Fernandes, R. A. De Sousa, Motorcycle helmets—a state of the art review, Accident Analysis & Prevention 56 (2013) 1–21.

[25] Z. Xiao, L. Wang, Y. Zhang, C. Yang, A study on motorcyclist head reponses during impact against front end of vehicle, International Journal of Crashworthiness (2020) 1–13.

[26] W. Gao, X. Liu, S. Chen, T. Q. Bui, S. Yoshimura, A cohesive zone based DE/FE coupling approach for interfacial debonding analysis of laminated glass, Theoretical and Applied Fracture Mechanics 108 (2020) 102668.

[27] W. Gao, M. Zang, The simulation of laminated glass beam impact problem by developing fracture model of spherical DEM, Engineering Analysis with Boundary Elements 42 (2014) 2–7.

[28] W. Gao, M. Zang, W. Xu, An approach to freely combining 3D discrete and finite element methods, International Journal of Computational Methods 11 (2014) 1350051.

[29] W. Gao, J. Wang, S. Yin, Y. Feng, A coupled 3D isogeometric and discrete element approach for modelling interactions between structures and granular matters, Computer Methods in Applied Mechanics and Engineering 354 (2019) 441–463.

[30] W. Xu, M. Zang, W. Gao, Adaptive combined DE/FE algorithm for brittle fracture of plane stress problems, Computational Mechanics 54 (2014) 535–546.

[31] Z. Lei, M. Zang, An approach to combining 3d discrete and finite element methods based on penalty function method, Computational Mechanics 46 (2010) 609–619.

[32] P. Del Linz, P. Hooper, H. Arora, D. Smith, L. Pascoe, D. Cormie, B. Blackman, J. Dear, Reaction forces of laminated glass windows subject to blast loads, Composite Structures 131 (2015) 193–206.

[33] Y. Peng, J. Yang, C. Deck, R. Willinger, Finite element modeling of crash test behavior for windshield laminated glass, International Journal of Impact Engineering 57 (2013) 27–35.

[34] P. Hooper, R. Sukhram, B. Blackman, J. Dear, On the blast resistance of laminated glass, International Journal of Solids and Structures 49 (2012) 899–918.

[35] M. Timmel, S. Kolling, P. Osterrieder, P. Du Bois, A finite element model for impact simulation with laminated glass, International Journal of Impact Engineering 34 (2007) 1465–1478.

[36] P. Du Bois, S. Kolling, W. Fassnacht, Modelling of safety glass for crash simulation, Computational materials science 28 (2003) 675–683.

[37] J. Wang, R. Wang, W. Gao, S. Chen, C. Wang, Numerical investigation of impact injury of a human head during contact interaction with a windshield glazing considering mechanical failure, International Journal of Impact Engineering (2020) 103577.

[38] W. Gao, R. Wang, S. Chen, M. Zang, An intrinsic cohesive zone approach for impact failure of windshield laminated glass subjected to a pedestrian headform, International Journal of Impact Engineering 126 (2019) 147–159.

[39] W. Gao, J. Xiang, S. Chen, S. Yin, M. Zang, X. Zheng, Intrinsic cohesive modeling of impact fracture behavior of laminated glass, Materials & Design 127 (2017) 321–335.

[40] S. Chen, M. Zang, D. Wang, Z. Zheng, C. Zhao, Finite element modelling of impact damage in polyvinyl butyral laminated glass, Composite Structures 138 (2016) 1–11.

[41] S. Chen, M. Zang, W. Xu, A three-dimensional computational framework for impact fracture analysis of automotive laminated glass, Computer Methods in Applied Mechanics and Engineering 294 (2015) 72–99.

[42] A. Esmaili, F. Taheri-Behrooz, Effect of cohesive zone length on the delamination growth of the composite laminates under cyclic loading, Engineering Fracture Mechanics 237 (2020) 107246.

[43] S. Azhdari, S. Fakhreddini-Najafabadi, F. Taheri-Behrooz, An experimental and numerical investigation on low velocity impact response of glares, Composite Structures 271 (2021) 114123.

[44] M. Ghajari, U. Galvanetto, L. Iannucci, R. Willinger, Influence of the body on the response of the helmeted head during impact, International journal of crashworthiness 16 (2011) 285–295.

[45] M. Ghajari, S. Peldschus, U. Galvanetto, L. Iannucci, Effects of the presence of the body in helmet oblique impacts, Accident Analysis & Prevention 50 (2013) 263–271.

[46] P. P. Camanho, C. G. Dávila, Mixed-mode decohesion finite elements for the simulation of delamination in composite materials, NASA/TM-2002-211737 pp (2002) 1–37.

[47] P. W. Harper, S. R. Hallett, Cohesive zone length in numerical simulations of composite delamination, Engineering Fracture Mechanics 75 (2008) 4774–4792.

[48] P. P. Camanho, C. Davila, M. De Moura, Numerical simulation of mixed-mode progressive delamination in composite materials, Journal of Composite Materials 37 (2003) 1415–1438.

[49] A. Turon, P. Camanho, J. Costa, C. D¨¢vila, A damage model for the simulation of delamination in advanced composites under variable-mode loading, Mechanics of Materials 38 (2006) 1072–1089.

[50] M. L. Benzeggagh, M. Kenane, Measurement of mixed-mode delamination

fracture toughness of unidirectional glass/epoxy composites with mixed-mode bending apparatus, Composites Science and Technology 56 (1996) 439–449.

[51] J. Mahmud, C. Holt, S. Evans, N. F. A. Manan, M. Chizari, A parametric study and simulations in quantifying human skin hyperelastic parameters, Procedia Engineering 41 (2012) 1580–1586.

[52] R. W. Ogden, Non-linear elastic deformations, Courier Corporation, 1997.

[53] J. O. Hallquist, et al., Ls-dyna theory manual, Livermore Software Technology Corporation (2006).

[54] M. Mansourinik, F. Taheri-Behrooz, The effect of interface debonding on flexural behaviour of composite sandwich beams, Journal of Sandwich Structures & Materials 22 (2020) 1132–1156.

[55] H. Fallahi, F. Taheri-Behrooz, A. Asadi, Nonlinear mechanical response of polymer matrix composites: a review, Polymer Reviews 60 (2020) 42–85.

[56] F. Taheri-Behrooz, H. S. Moghaddam, Nonlinear numerical analysis of the v-notched rail shear test specimen, Polymer Testing 65 (2018) 44–53.

[57] I. Lapczyk, J. A. Hurtado, Progressive damage modeling in fiber-reinforced materials, Composites Part A: Applied Science and Manufacturing 38 (2007) 2333–2341.

[58] N. J. Mills, S. Wilkes, S. Derler, A. Flisch, Fea of oblique impact tests on a motorcycle helmet, International Journal of Impact Engineering 36 (2009) 913–925.

[59] D. Systèmes, ABAQUS analysis User's Guide 6.14, 2014.

[60] J. Pelfrene, S. V. Dam, W. V. Paepegem, Numerical analysis of the peel test for characterisation of interfacial debonding in laminated glass, International Journal of Adhesion and Adhesives 62 (2015) 146 – 153.

[61] J. Xu, Y. Li, X. Chen, Y. Yan, D. Ge, M. Zhu, B. Liu, Characteristics of windshield cracking upon low-speed impact: Numerical simulation based on the extended finite element method, Computational Materials Science 48 (2010) 582 – 588.

[62] H. Yuan, X. Li, Effects of the cohesive law on ductile crack propagation simulation by using cohesive zone models, Engineering Fracture Mechanics 126 (2014) 1 – 11.

[63] J. O. Aguilar, J. M. Rodríguez-Lelis, M. Carrasco de la Fuente, C. López-Mata, J. A. Arellano-Cabrera, F. Chan, Adhesion strength in laminated glazings containing multilayer solar control coatings, Journal of Mechanical Science and Technology 26 (2012) 1725–1730.

[64] B. Krour, F. Bernard, S. Benyoucef, B. Fahsi, Influence of the lamination on the redundancy of a horizontally layered glass element and analysis of the debonding of the adhesive interlayer, International Journal of Adhesion and Adhesives 64 (2016) 116 – 127.

[65] D. Karagiozova, R. Mines, Impact of aircraft rubber tyre fragments on aluminium alloy plates: Ii—numerical simulation using ls-dyna, International Journal of Impact Engineering 34 (2007) 647–667.

[66] Y. Peng, Y. Chen, J. Yang, D. Otte, R. Willinger, A study of pedestrian and bicyclist exposure to head injury in passenger car collisions based on accident data and simulations, Safety Science 50 (2012) 1749–1759.

[67] J. Chen, A study on helmet protective performance for head injury based on motorcycle accident reconstruction, Master's thesis, Hunan University, 2013.

[68] Y. Matsui, S. Oikawa, N. Hosokawa, Effectiveness of wearing a bicycle helmet for impacts against the front of a vehicle and the road surface, Traffic injury prevention 19 (2018) 773–777.

[69] M. Ghajari, U. Galvanetto, L. Iannucci, Influence of the body on kinematic and tissue level head injury predictors in motorcyclists accidents, in: Proceedings of IRCOBI Conference, York, UK, 2009, pp. 9–11.

[70] L. Di Landro, G. Sala, D. Olivieri, Deformation mechanisms and energy absorption of polystyrene foams for protective helmets, Polymer testing 21 (2002) 217–228.

[71] S. Meng, A. Cernicchi, S. Kleiven, P. Halldin, The biomechanical differences of shock absorption test methods in the us and european helmet standards, International journal of crashworthiness 24 (2019) 399–412.

Wei Gao: Conceptualization, Methodology, Writing - original draft and Writing - Review & Editing; Jiawen Wang: Investigation, Validation and Data Curation; Xiaoqiang He: Software, Investigation and Visualization; Y.T. Feng: Methodology and Writing - Review & Editing; Shunhua Chen: Methodology; Chengyong Wang: Resources

Declaration of interests

☒ The authors declare that they have no known competing financial interests or personal relationships that could have appeared to influence the work reported in this paper.

☐The authors declare the following financial interests/personal relationships which may be considered as potential competing interests: